RESEARCH ARTICLE

Large-eddy simulation of soil moisture heterogeneity-induced secondary circulation with ambient winds

Lijie Zhang[1] | **Stefan Poll**[1,2,3] | **Stefan Kollet**[1,2,3]

[1]Institute for Bio- and Geosciences: Agrosphere (IBG-3), Research Centre Jülich, Jülich, Germany

[2]SimDataLab Terrestrial Systems, Jülich Supercomputing Centre (JSC), Jülich, Germany

[3]Centre for High-Performance Scientific Computing in Terrestrial Systems, Geoverbund ABC/J, Jülich, Germany

Correspondence
Lijie Zhang, Forschungszentrum Jülich IBG-3, Wilhelm-Johnen-Straße, 52428 Jülich, Germany.
Email: l.zhang@fz-juelich.de

Abstract

Land surface heterogeneity in conjunction with ambient winds influences the convective atmospheric boundary layer by affecting the distribution of incoming solar radiation and forming secondary circulations. This study performed coupled large-eddy simulation (ICON-LEM) with a land surface model (TERRA-ML) over a flat river corridor mimicked by soil moisture heterogeneity to investigate the impact of ambient winds on secondary circulations. The coupled model employed double-periodic boundary conditions with a spatial scale of 4.8 km. All simulations used the same idealized initial atmospheric conditions with constant incident radiation of 700 W·m^{-2} and various ambient winds with different speeds (0 to 16 m·s^{-1}) and directions (e.g., cross-river, parallel-river, and mixed). The atmospheric states are decomposed into ensemble-averaged, mesoscale, and turbulence. The results show that the secondary circulation structure persists under the parallel-river wind conditions independently of the wind speed but is destroyed when the cross-river wind is stronger than 2 m·s^{-1}. The soil moisture and wind speed determine the influence on the surface energy distribution independent of the wind direction. However, secondary circulations increase advection and dispersive heat flux while decreasing turbulent energy flux. The vertical profiles of the wind variance reflect the secondary circulation, and the maximum value of the mesoscale vertical wind variance indicates the secondary circulation strength. The secondary circulation strength positively scales with the Bowen ratio, stability parameter ($-Z_i/L$), and thermal heterogeneity parameter under cross-river wind and mixed wind conditions. The proposed similarity analyses and scaling approach provide a new quantitative perspective on the impact of the ambient wind under heteronomous soil moisture conditions on secondary circulation.

KEYWORDS

ambient winds, Bowen ratio, land surface model, large-eddy simulation, moisture spatial heterogeneity, secondary circulation, similarity theory, turbulence

1 | INTRODUCTION

Land surface heterogeneity influences the convective atmospheric boundary layer (CBL) by inducing secondary circulations (SCs) and affects the convective energy, mass, and momentum transfer (Pielke Sr, 2001; Patton *et al.*, 2005; Kang *et al.*, 2007; Prabha *et al.*, 2007; Kang, 2009; Poll *et al.*, 2017; Lee *et al.*, 2019; Stoll *et al.*, 2020). The eddy-covariance measurements from a single flux tower underestimate the heat flux by about 10% to 30%, mainly due to dispersive fluxes and advection caused by SCs, which are not captured in observations (Mauder *et al.*, 2020; Wanner *et al.*, 2022). On the other hand, SCs overestimate heat fluxes by up to 15%–25% if the site is in constant roll circulation (Prabha *et al.*, 2007). Current large-scale models use subgrid-scale parameterization for the unresolved part of the variances. A comprehensive investigation of the land surface heterogeneity-induced SCs under ambient winds improves the understanding of the surface layer processes and the performance of large-scale models, for example, numerical weather prediction.

Many efforts in the community have gone into identifying the effects from the (sub-)meso-scale on the lower atmosphere boundary layer through field measurements. Several experimental studies have been carried out, such as High Definition of Clouds and Precipitation for Advancing Climate Prediction (HD[CP]²) (Stamnas *et al.*, 2016; Macke *et al.*, 2017), Lindenberg Inhomogeneous Terrain Fluxes between Atmosphere and Surface (LITFASS-2003) (Beyrich and Mengelkamp, 2006; Foken *et al.*, 2010), the International H₂O project (IHOP_2002) (Weckwerth *et al.*, 2004), the Horizontal Array Turbulence Study experiment (HATS) (Hatlee and Wyngaard, 2007), the Canopy Horizontal Array Turbulence Study (CHATS) (Dupont and Patton, 2012), the Idealized Planner-Array Study for Quantifying Surface heterogeneity (IPAQS) (Morrison *et al.*, 2022), the CHEESEHEAD19 (Butterworth *et al.*, 2021; Sedlar *et al.*, 2022), the Land–Atmosphere Feedback Experiment (LAFE) (Behrendt *et al.*, 2018) and many others. In recent field campaigns, more focus has been placed on capturing spatial energy fluxes and attempting to close the surface energy balance (SEB) gap under heterogeneous land cover and complex terrain. Based on the high-frequency measurement, Gao *et al.* (2017) proposed a phase lag between the vertical wind and water vapour density associated with the SC, which lead to an underestimation of latent heat flux.

Using model simulations to examine SCs has become a powerful line of research, because the simulation results provide spatially distributed information at a high temporal resolution under a controlled environment (Wanner *et al.*, 2022), which, currently, cannot be obtained by measurements. The rapid development of high-performance computing (HPC) systems enables Large-eddy simulation (LES) to characterize and quantify the energy-containing turbulence constituting a promising approach for studying the CBL turbulent processes. Kanda *et al.* (2004) found a slow-moving turbulent organized structure over the homogeneous land surface. For this reason, it has been proposed in the literature that the fluxes averaged over longer periods or larger spatial coverage could close the SEB (Oncley *et al.*, 2007; Foken *et al.*, 2010). In addition, land surface heterogeneity can also explain the surface energy balance issue, and more work has revealed the effect of SC on heterogeneous surfaces on the SEB problem (Eder *et al.*, 2015).

A plethora of studies focused on the impact of heterogeneity scale (λ) and amplitude on the formation of SC (Avissar and Schmidt, 1998; Raasch and Harbusch, 2001; Letzel and Raasch, 2003; Patton *et al.*, 2005; Han *et al.*, 2019b). A significant effect of land surface heterogeneity on the atmosphere is only observed when λ approaches the CBL height (Zi) (Raasch and Harbusch, 2001). Researchers have reported various values for the optimal heterogeneity scale, for example, four times Z_i, approximately 4–6 km (Schumann, 1991); 4–9 times Z_i (Patton *et al.*, 2005); ~20–40 km (Avissar and Schmidt, 1998) Han *et al.*, (2019b) indicated that the strongest horizontal and vertical transport occurs when λ is 19.2 and 2.4 km, respectively. The heterogeneity amplitude also affects the SCs (Kang and Bryan, 2011; Prabha *et al.*, 2007; van Heerwaarden and de Arellano, 2008). Prabha *et al.* (2007) studied the heterogeneity-induced SC and found that a reduced heat flux leads to a shallower circulation. van Heerwaarden and de Arellano (2008) showed that the greater the heterogeneity amplitude, the stronger the SC. Kang and Bryan (2011) also reported an earlier commencement of convection with increased heterogeneity amplitude.

In addition to the heterogeneity scale and amplitude, the ambient wind (i.e., background wind) also influences the formation of the SC (Lee *et al.*, 2019). Previous studies showed that ambient wind speed affects SC's strength, location and structure (Prabha *et al.*, 2007). Avissar and Schmidt (1998) proposed that the impact of a weak ambient wind of 2.5 m·s⁻¹ is not negligible on the SC and a moderate ambient wind speed of 5 m·s⁻¹ is strong enough to eliminate the effect of the surface heterogeneity in their simulations. The LES result from Eder *et al.* (2015) also shows that with the ambient of 6 m·s⁻¹, the vertical velocity field is no longer related to surface heterogeneity over a desert–forest heterogeneity at a scale of 24 km. Kang and Lenschow (2014) studied the impact of ambient wind (5 m·s⁻¹) at a large heterogeneity scale ($\lambda = 32$ km) and showed that the effect of surface heterogeneity reduced

along the ambient wind direction. However, Raasch and Harbusch, (2001) demonstrated that circulation structures persist even at ambient winds of 7.5 m·s⁻¹ in their simulation. The orientation of the surface heterogeneity and wind direction are different in those simulations. The ambient wind in Raasch's simulation is perpendicular to the direction of surface heterogeneity, while the ambient wind is aligned diagonally with the surface pattern in Raasch and Harbusch (2001) and Eder *et al.* (2015). Another reason is that the three-dimensional structure of the SC is very complex (Prabha *et al.*, 2007). Lee *et al.* (2019) pointed out that SC no longer exists when the ambient wind is stronger than the mesoscale horizontal wind.

Dimensional and similarity analysis has been widely used in the community to explore the self-similarity of the CBL characteristics and simplify the complicated physical process through parameterization. As one example, the Monin–Obukhov similarity theory (MOST) describes the empirical relationship between the non-dimensional scalars and fluxes of the surface layer (Holtslag and Nieuwstadt, 1986). MOST applies the logarithmic wind and temperature profile as a function of the atmosphere's stability by assuming a homogeneous land surface. In the last decades, numerous field and numerical experiments showed the reliability of MOST (Foken, 2006; Kang *et al.*, 2007; Fortuniak *et al.*, 2013; Ding and Tong, 2021). Recently, Margairaz *et al.*, 2020 proposed the thermal heterogeneity parameter, which denotes the ratio of buoyancy to inertial forces, to indicate whether the land surface heterogeneity impacts the atmosphere. However, questions regarding the self-similarity of the impact of ambient winds on the SC have not been addressed.

This study aims to provide a new quantitative perspective on the impact of ambient wind under heterogeneous soil moisture conditions on the formation of SC, and vertical profiles, with an emphasis on the relationship between the SC strength and appropriate scaling parameters and its implication on the SEB. The paper is organized as follows: Section 2 explains the methodology, including a detailed description of the ICOsahedral Non-hydrostatic (ICON) model, the simulation setup, and the scaling parameters. Section 3 presents the results and discussions, followed by the summary and conclusion in Section 4.

2 | METHODOLOGY

Section 2.1 introduces the LES model, including the coupled land surface model and the essential equations for calculating the exchange heat flux. Section 2.2 explains the simulation and numerical experimental setup,

including the model domain, time step, duration, atmospheric conditions, and ambient winds. Section 2.3 presents the scaling parameters and decomposition strategy for further analysis.

2.1 | Model description

The ICON model is a fully compressible atmospheric model developed jointly by the German Weather Service (DWD) and the Max Planck Institute of Meteorology (MPI-M) (Cioni and Hohenegger, 2017; Dipankar *et al.*, 2015; Heinze *et al.*, 2017; Wan *et al.*, 2013; Zängl *et al.*, 2015). ICON uses geodesic Delaunay grids with C-type staggering and consists of three modes: numerical weather and climate prediction, and LES, constituting the next-generation unified modelling system. The ICON large-eddy model (ICON-LEM) applied in this study implements the modified Smagorinsky turbulence scheme to account for thermal stratification (Lilly, 1962). For more details on ICON-LEM, the interested reader is referred to Dipankar *et al.*, 2015, Heinze *et al.*, 2017 and Zängl *et al.*, 2015.

To account for the feedback with the land surface, we apply the TERRA-Multi Layer (TERRA-ML) model (Grasselt *et al.*, 2008; Schrodin and Heise, 2001; Schulz and Vogel, 2020) coupled with ICON-LEM to provide moisture, heat and momentum fluxes as the lower boundary conditions of the atmosphere. In the following, we provide the equations of the essential energy-moisture fluxes at the land surface. The bulk aerodynamic method is used to calculate the sensible heat flux (SH):

$$\text{SH} = \rho C_p C_h |U| (\theta \pi_{\text{sfc}} - T_{\text{sfc}}), \qquad (1)$$

where ρ is the air density (kg·m⁻³), C_p is the heat capacity (J·K⁻¹·kg⁻¹), C_h is the bulk transfer coefficient for sensible heat at the surface, $|U|$ is the absolute horizontal wind speed (m·s⁻¹), θ is air potential temperature (K) at the lowest level of the atmospheric model, π_{sfc} is scaled pressure at the surface, and T_{sfc} is the ground surface temperature (K). We only simulate the bare soil without vegetation cover. TERRA-ML applies the resistance formulation (Schulz and Vogel, 2020) to calculate the latent heat flux (LH) of soil evaporation, which improved the model performance more than the original Biosphere-Atmosphere Transfer Scheme (BATS) (Dickinson, 1984).

$$\text{LH} = \rho \frac{1}{r_a + r_s} (q_v - q_{\text{sat}}) L_v, \qquad (2)$$

where r_a is aerodynamic resistance (s·m⁻¹), r_s is the soil resistance (s·m⁻¹), q_v is the specific humidity (kg·kg⁻¹) at
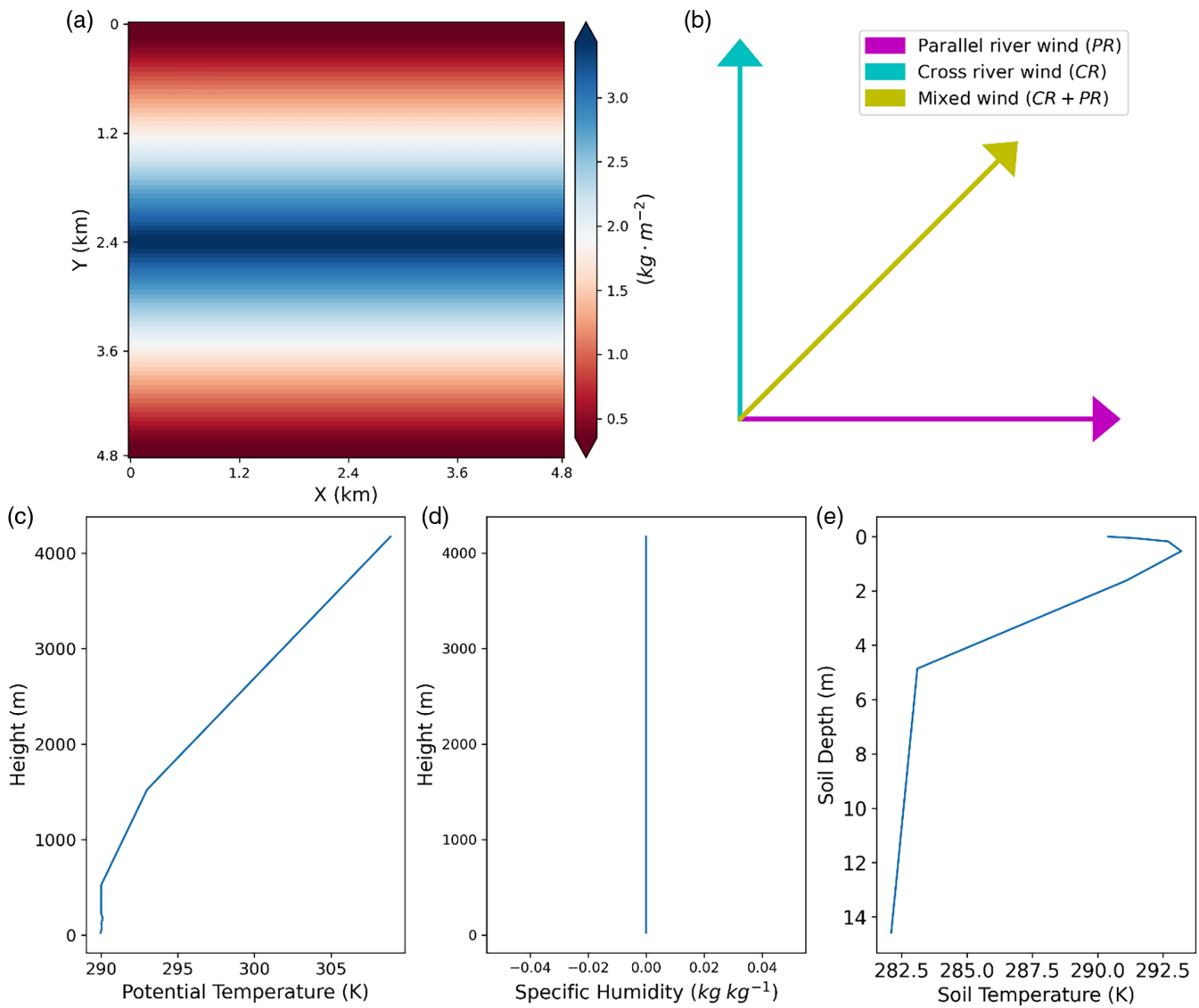
FIGURE 1 (a). Initial surface soil moisture. Continuous gradient soil moisture distribution crosses the river with wet soil in the middle and dry soil at the edge, mimicking a river corridor. (b). Parallel-river (PR) wind in the x-direction; cross-river (CR) wind in the y-direction. (c) Initial potential temperature profile. (d) Initial specific humidity profile. (e) Initial soil temperature profile [Colour figure can be viewed at wileyonlinelibrary.com]

the lowest atmospheric layer, and q_{sat} is the saturated specific humidity (kg·kg^{-1}) at the surface, L_v is the latent heat of vapourization (J·kg^{-1}). Interested readers are referred to Schulz *et al.*, 1998 and Schulz and Vogel, 2020 for more details.

The ground heat flux (G) governs the soil temperature at the top surface layer based on the heat conduction equation (Grasselt *et al.*, 2008). TERRA-ML has eight soil layers, with the depth of the lower boundary varying from 0.01 to 15 m (Davin *et al.*, 2011; Han *et al.*, 2019b). We turn off the soil moisture dynamics in the simulations to limit potential feedback mechanisms and keep the problem tractable.

2.2 | Simulation and numerical experimental setup

A spatial soil moisture distribution is defined to mimic a river corridor with wet soils in the centre and continuously drying in the direction of the edge (see Figure 1a). The detailed setup has already been described and used by Han *et al.*, (2019b). We set a uniform bare soil surface with flat terrain to avoid additional uncertainties caused by land use (Prabha *et al.*, 2007; Poll *et al.*, 2022) or complex terrain (Rihani *et al.*, 2015). In the numerical experiments, we apply ambient winds to the domain with wind speeds varying from 0 to 16 m·s^{-1} and wind direction

TABLE 1 Ambient winds of different simulations

Simulations	PR wind speed	CR wind speed
Reference simulation	PR = 0 m·s⁻¹	CR = 0 m·s⁻¹
PR wind simulation	PR = 0, 0.25, 0.5, 1, 2, 4, 8, 16 m·s⁻¹	CR = 0 m·s⁻¹
CR wind simulation	PR = 0 m·s⁻¹	CR = 0, 0.5, 1, 2, 4, 8, 16 m·s⁻¹
Mixed wind simulation	PR = CR = 0.35, 0.70, 1.41, 2.83, 5.66, 11.3 m·s⁻¹	
PR wind simulation with a fixed minor CR wind	PR = 2, 4, 8, 16 m·s⁻¹	CR = 0.75 m·s⁻¹

between cross-river (CR) and parallel-river (PR), or mixed (CR + PR) (see Figure 1b).

The atmospheric domain size is $4.8 \times 4.8 \times 4.2$ km with $96 \times 96 \times 84$ grid cells in the x, y, and z directions, respectively. The horizontal and vertical pixel sizes are 50 m ($\Delta_x = \Delta_y = \Delta_z = 50$ m), and the model time step is 0.5 s. The land surface model is set to match the size of the atmospheric domain with a coverage of 4.8×4.8 km in each horizontal soil layer. The horizontal domain is closed by double-periodic boundary conditions. All simulations utilize the same atmospheric and land surface initial conditions. The Initial potential temperature is constant (290 K) below 525 m, increases at a rate of 3 K·km⁻¹ between 525 m and 1,525 m, and 6 K·km⁻¹ above 1,525 m (Figure 1c). The atmosphere is dry with zero specific humidity (Figure 1d), and the incoming radiation at the top of the atmosphere is constant at 700 W·m⁻². Table 1 lists the ambient winds for different simulations. The ambient wind is kept constant during the 12 h simulation. The Coriolis effect is not considered in this study. The output frequency is set to 900 s, while in addition exporting atmospheric scalars for the lowest atmosphere layer for calculating space mean advection, dispersive and turbulent energy fluxes at the model time step.

The simulation with no ambient wind (PR = CR = 0 m·s⁻¹) serves as a reference in the analyses. In addition to the aforementioned CR, PR, and CR + PR simulations varying from 0 to 16 m·s⁻¹, we run several simulations with various PR winds and a fixed minor CR wind (PR > 0, CR = *0.75* m·s⁻¹) to facilitate a more in-depth study of the effect of the ambient wind direction on the CBL.

2.3 | Scaling parameters and decomposition

In boundary layer meteorology, the similarity theory assumes that scaling parameters can universally characterize the CBL based on several simplifying assumptions (Franssen *et al.*, 2010), such as the homogeneous land surface and the zero-sum of vertical wind (Holtslag and Nieuwstadt, 1986). This study utilizes the commonly used

scaling parameters, including convective velocity scale ($w*$), friction velocity ($u*$), Obukhov length (L), and the recently proposed thermal heterogeneity parameter, to study the SC strength quantitatively.

The convective velocity scale ($w*$), also known as the Deardorff velocity, is approximately the updraft speed related to the buoyancy-controlled diffusion in the CBL (Deardorff, 1970).

$$w* = \left(\frac{g}{T} \cdot \overline{w'\theta'} \cdot Z_i \right)^{1/3},$$ (3)

where g is the gravitational acceleration (m·s⁻²), Z_i is the CBL height, T is the absolute temperature, w' and θ' are the fluctuation of vertical wind and potential temperature, respectively. $\overline{w'\theta'}$ (K · m · s⁻¹) is the turbulent energy flux, and $\frac{g}{T} \cdot \overline{w'\theta'}$ is denoted as the buoyancy flux leading to the velocity scale, where the overline indicates the time average.

The friction velocity is another commonly used scaling parameter representing the shear stress velocity due to mechanical turbulence (Weber, 1999).

$$u* = \left(\overline{u'w'}^2 + \overline{v'w'}^2 \right)^{1/4},$$ (4)

The Obukhov length (L) is a parameter with a dimension of length that links the friction velocity and buoyancy flux, and k is the von-Karman constant with an approximate value of 0.40.

$$L = \frac{u*^3}{k\frac{g}{T}\overline{w'\theta'}_s}$$ (5)

The thermal heterogeneity parameter proposed by Margairaz *et al.* (2020) is expressed as

$$H_{\text{par}} = \frac{gl_{\text{h}}}{U^2} \frac{\Delta T}{\overline{T}},$$ (6)

where l_{h} is the length scale of the surface thermal heterogeneities, which is $l_{\text{h}} = \lambda = 4.8$ km in our simulation. ΔT is the spatial mean value of the absolute difference between the point to the spatial average air temperature,

which can be expressed as $\Delta T = <| T_s - < T_s >|>$, where the angled brackets indicate the spatial average. The interested reader is referred to the work of Margairaz *et al.* (2020).

This study utilizes the commonly used scale decomposition scheme to separate the atmospheric variables (e.g., wind speed) into ensemble average ($\langle f \rangle(z)$), mesoscale ($f_m(y,z)$), and turbulence ($f'(x,y,z,t)$), respectively (Raasch and Harbusch, 2001; Patton *et al.*, 2005; Shen *et al.*, 2016; Han *et al.*, 2019b)

$$f(x,y,z,t) = \langle f \rangle(z) + f_m(y,z) + f'(x,y,z,t), \quad (7)$$

To investigate the impact of SC on the proportion of SEB, the total heat flux is decomposed into a spatial mean, the corresponding fluctuation and bulk advection using Equation 8 (Morrison *et al.*, 2022). We applied the decomposition at the lowest atmosphere layer (i.e., 25 m above ground level)

$$\langle \overline{w\theta} \rangle = \langle \overline{w}\,\overline{\theta} \rangle + \left\langle \overline{w''\theta''} \right\rangle + \left\langle \overline{w'\theta'} \right\rangle. \quad (8)$$

Here, the terms on the right-hand side are advection, dispersive and turbulent energy flux, respectively. The advection must be considered, as the mean vertical wind component of steady flow does not equal zero. The dispersive flux is the spatial mean of covariance between the spatial fluctuation of vertical velocity and potential temperature, where the double prime indicates the spatial fluctuation from the spatial mean.

3 | RESULTS AND DISCUSSION

Section 3.1 compares the impact of different ambient wind speeds and directions on the CBL structure and the essential bulk properties of each simulation. Section 3.2 focuses on the influence of ambient wind on the distribution of surface heat fluxes and the temporal evolution of advection, dispersive and turbulent energy flux. Section 3.3 explores CBL characteristics by inspecting the vertical profile variance of vertical wind, horizontal wind, and potential temperature. Section 3.4 investigates the relationship of SC strength with the Bowen ratio (SH and LH ratio), $-Z_i/L$ (CBL height and Obukhov length ratio), and the thermal heterogeneity parameter.

3.1 | SC structure

A well-organized SC structure is observed in the CBL for the reference simulation, which was repeated in this study following Han *et al.*, (2019b) and is shown in Figure 2 for completeness. Similar to the previous research (Avissar and Schmidt, 1998; Patton *et al.*, 2005; Poll *et al.*, 2022; Raasch and Harbusch, 2001), the narrow and strong updraft appears over the dry soil at the edge, and a broader but weaker downdraft appears over the wet soil in the centre. Here, we focus on the impact of the ambient wind on the SC formation (Figures 3, 4) and the essential statistics (Figure 5).

The first column in Figure 3 shows the mesoscale vertical wind under PR wind conditions (PR > 0, CR = 0 m·s^{-1}) with a narrow updraft at the edge and a downdraft in the centre. The structure of the SC is not destroyed by the PR wind, even for high wind speeds (e.g., 16 m·s^{-1}). In contrast, the second column of Figure 3 shows that CR wind strongly impacts SC formation. For low wind velocities (e.g., CR = 0.5, 1 m·s^{-1}), a weaker SC structure is shifted along the wind direction due to the periodic boundary condition. The shifting distance increases with the increase of CR wind speed. SC strength decreases with increased CR wind, and SC vanishes when CR > 2 m·s^{-1}. The third column of Figure 3 also shows the result of mixed
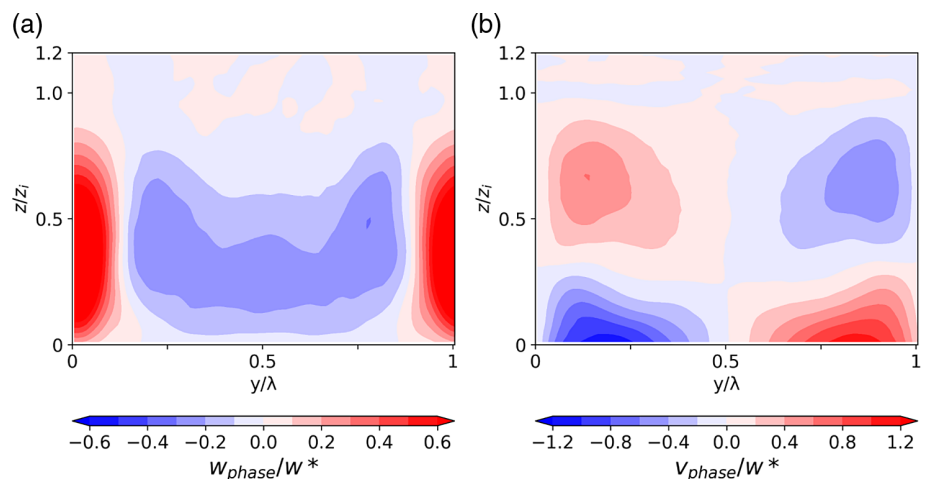
FIGURE 2 Vertical cross-section (y–z) of mesoscale vertical wind (a) and mesoscale horizontal wind (b) over the period of 1–12 h under simulation without ambient wind [Colour figure can be viewed at wileyonlinelibrary.com]
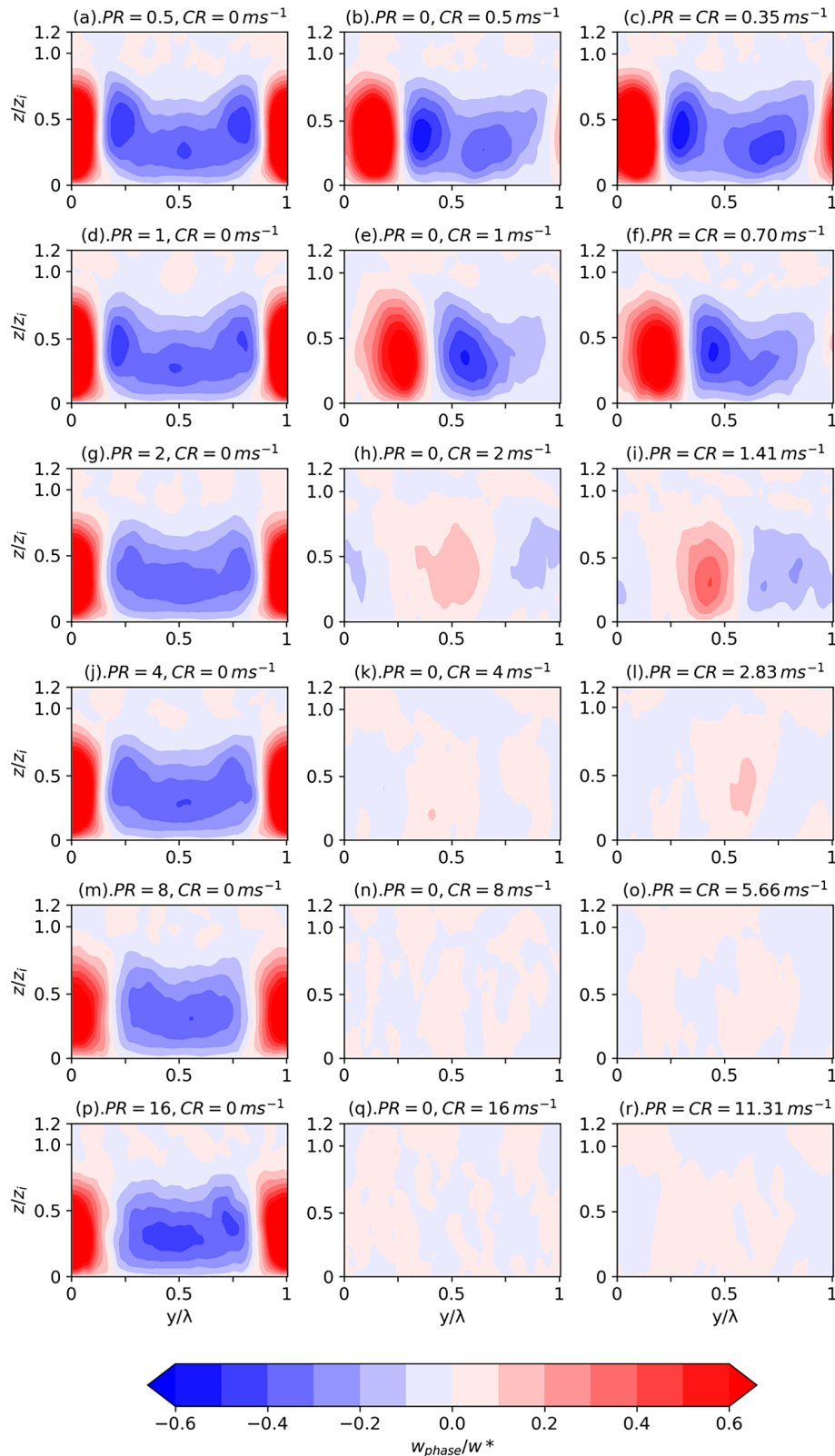
FIGURE 3 Vertical cross-section (y–z) of mesoscale vertical wind over the period of 1–12 h under varying ambient wind conditions. The first column depicts the simulation results under the parallel-river wind (PR > 0.0, CR = 0.0 m·s^{-1}), the second column is the cross-river wind (PR = 0.0, CR > 0.0 m·s^{-1}), and the third column is the mixed wind (PR = CR > 0.0 m·s^{-1}); λ is the soil moisture heterogeneity scale of 4.8 km, and z is the height [Colour figure can be viewed at wileyonlinelibrary.com]

wind simulations (PR = CR). The CR wind component dominates the impact on the SC structure. A weak and shifted SC structure still exists at a wind speed of 2 m·s^{-1} in Figure 3i (PR = CR = 1.41 m·s^{-1}), but the SC structure vanishes in Figure 3l when PR = CR = 2.83 m·s^{-1}.

Figure 4 shows the mesoscale horizontal wind averaged over the period 1–12 h. PR wind does not significantly impact the SC structure, even for large wind speeds. In contrast, CR wind affects SC strongly. The strength of the SC structure decreases with the increase of CR wind speed

FIGURE 4 Vertical cross-section (y–z) of mesoscale horizontal wind (U) over the period of 1–12 h under varying ambient wind conditions. The first column is the simulation result under the parallel-river wind (PR > 0.0, CR = 0.0 m·s^{-1}), the second column is the cross-river wind (PR = 0.0, CR > 0.0 m·s^{-1}), and the third column is the mixed wind (PR > 0.0, CR > 0.0 m·s^{-1}); λ is the soil moisture heterogeneity scale of 4.8 km, and z is the height [Colour figure can be viewed at wileyonlinelibrary.com]
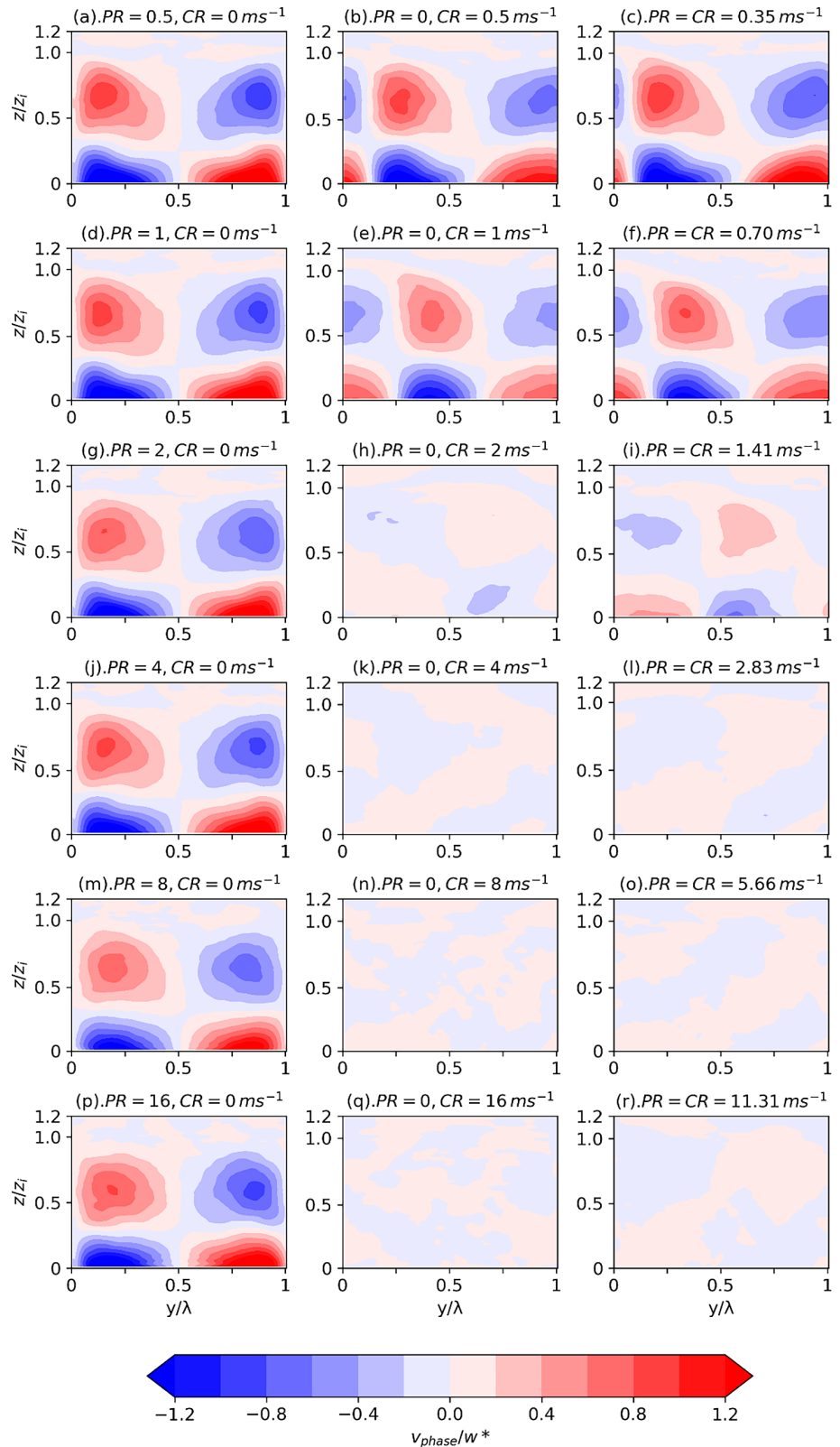
until the structure vanishes when $CR > 2$ m·s^{-1}. The air pressure decreases with the distance to the river due to air expansion over the warm surface and vice versa (see supplementary material, Figures S1–S3). The CR winds blend the air and destroy the air pressure structure. Because of the dry initial atmosphere setting, the specific humidity value is minimal, only affecting the lower CBL within the 12 simulation hours.

In terms of the surface energy fluxes, Figure 5 shows that SH and LH increase with increasing ambient wind
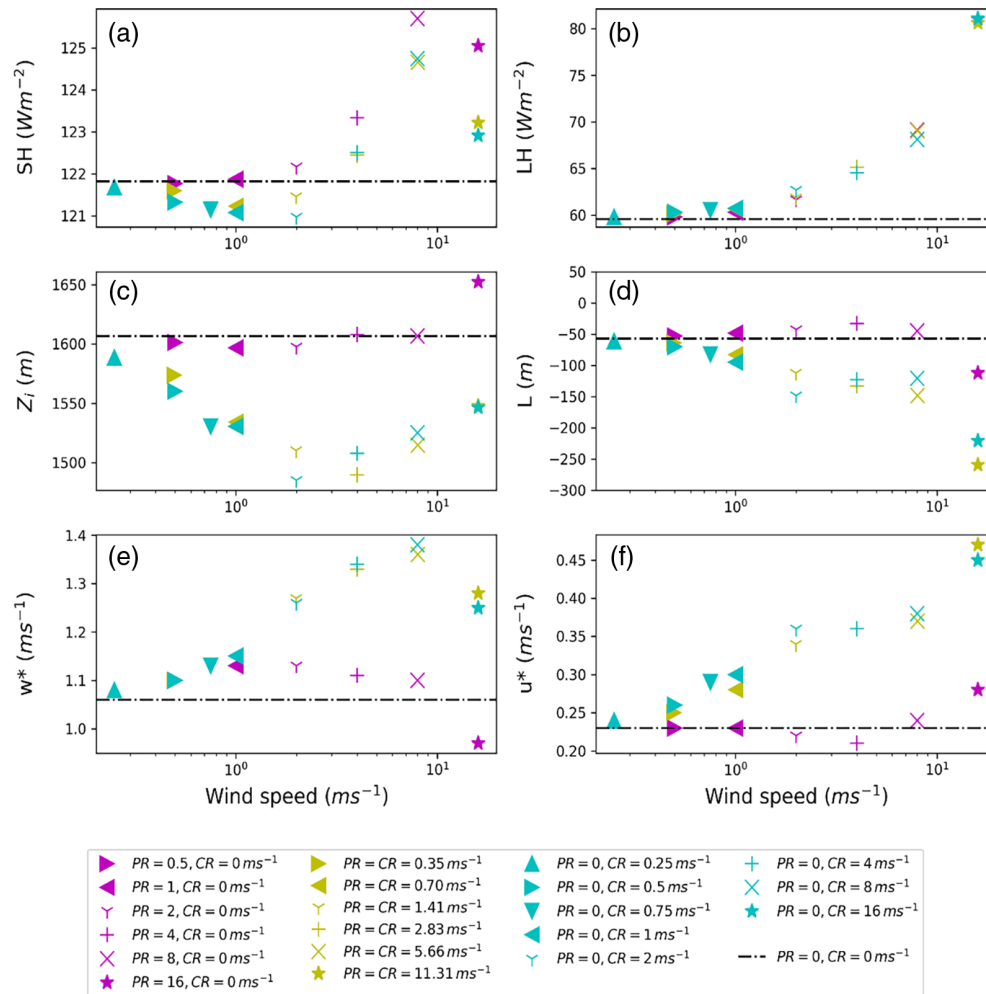
Legend:
- ▶ $PR = 0.5, CR = 0\,ms^{-1}$
- ◀ $PR = 1, CR = 0\,ms^{-1}$
- Y $PR = 2, CR = 0\,ms^{-1}$
- + $PR = 4, CR = 0\,ms^{-1}$
- ✕ $PR = 8, CR = 0\,ms^{-1}$
- ★ $PR = 16, CR = 0\,ms^{-1}$
- ▶ $PR = CR = 0.35\,ms^{-1}$
- ◀ $PR = CR = 0.70\,ms^{-1}$
- Y $PR = CR = 1.41\,ms^{-1}$
- + $PR = CR = 2.83\,ms^{-1}$
- ✕ $PR = CR = 5.66\,ms^{-1}$
- ★ $PR = CR = 11.31\,ms^{-1}$
- ▲ $PR = 0, CR = 0.25\,ms^{-1}$
- ▶ $PR = 0, CR = 0.5\,ms^{-1}$
- ▼ $PR = 0, CR = 0.75\,ms^{-1}$
- ◀ $PR = 0, CR = 1\,ms^{-1}$
- Y $PR = 0, CR = 2\,ms^{-1}$
- + $PR = 0, CR = 4\,ms^{-1}$
- ✕ $PR = 0, CR = 8\,ms^{-1}$
- ★ $PR = 0, CR = 16\,ms^{-1}$
- ─·─ $PR = 0, CR = 0\,ms^{-1}$

speed independent of the wind direction in the wet region, which is more pronounced for LH. This is because the parameterizations of SH and LH are based on wind speed (Equations 1, 2). In contrast, variables Z_i, L, w_*, and u_* show a dependence on wind speed and direction. The impact of PR wind on Z_i, L, w_*, and u_* is nearly negligible except for the simulation with PR = 16 m·s⁻¹. The impact of CR wind is evident in the intensity of u_*, which doubles from 0.23 to 0.46 m·s⁻¹ when the CR wind increases from 0 to 16 m·s⁻¹; in addition, L decreases from −52 to −250 m correspondingly.

The influence of CR wind speed on Z_i is non-linear. Z_i decreases with the increase of CR wind when CR ≤ 2 m·s⁻¹ and Z_i increases again with increasing CR wind (CR > 2 m·s⁻¹), Z_i reaches the minimum when CR = 2 m·s⁻¹. Interestingly, the maximum value of w_* is observed at CR = 8 m·s⁻¹. The attenuation of SCs in the simulation with CR wind imprints on the scaling parameters, whereas in the simulation of PR wind with persistent SCs, there is no relationship between the scaling parameters and SC.

3.2 | Land surface and atmospheric surface layer variables

Soil moisture controls the partitioning of incident solar radiation into SH *and* LH, and G, which results in spatial variability characterized by the minimum (maximum) LH on dry (wet) soils (Patton *et al.*, 2005; Han *et al.*, 2019b; Poll *et al.*, 2022). Here, we focus on the influence of ambient wind speed and direction on the surface energy distribution, and the advection, dispersive and turbulent energy fluxes at the lowest atmosphere layer (i.e., 25 m above ground level).

Figure 6 shows that the soil moisture and wind speed determine the cross section energy distribution at the surface independent of the wind direction. The impact of ambient wind on the heat flux amplitude is more evident in the wet centre than along the dry edges of the domain. With the increase of wind speed, SH increases slightly at the dry edge but decreases strongly in the centre, even to a negative value. Correspondingly, the increased wind speed increases the LH in the centre. However, LH remains
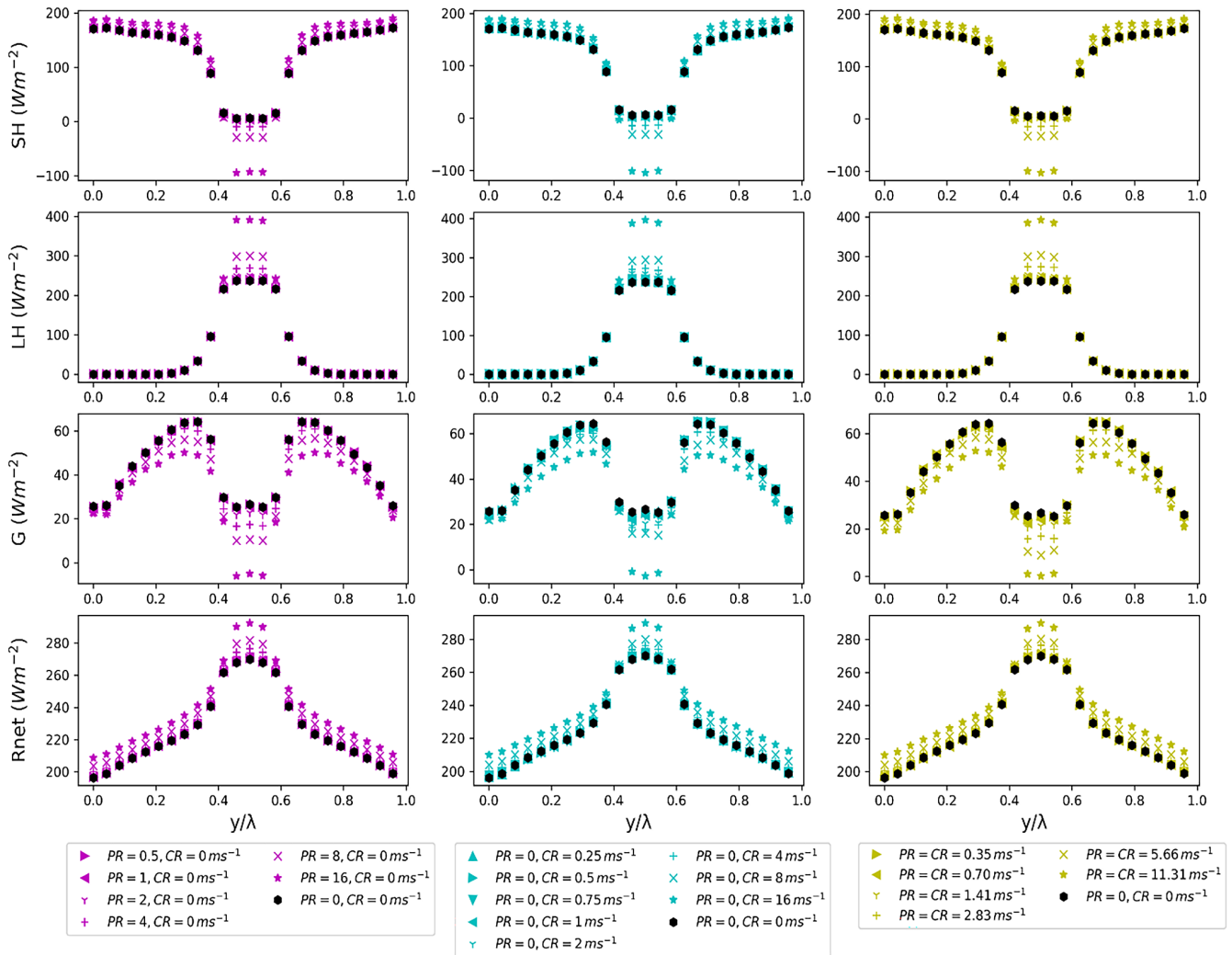
FIGURE 6 Cross-river surface energy flux. First row: SH over the period 1–12 h; second row: LH; third row: ground heat flux; fourth row: net radiation. The first column are for the simulation result with parallel-river (PR) wind, second column for the cross-river (CR) wind, third column for the mixed wind, and the black symbol represents the reference simulation with PR = CR = 0 m·s^{-1} [Colour figure can be viewed at wileyonlinelibrary.com]

constant at the dry edge as the low availability of soil moisture limits evaporation.

The increasing wind speed increases the domain-averaged R_{net} for all wind directions. The R_{net} difference between wet and dry soils becomes significant at higher wind speeds. For example, the increment in R_{net} over wet soils is around 20 W·m^{-2} when the ambient wind increases from 0 to 16 m·s^{-1}, while it is only about 10 W·m^{-2} for the dry soils.

Wind direction has a negligible effect on surface energy distribution but impacts the heat flux at the lowest atmosphere level. Figure 7a–c indicates the spatially averaged advection under PR winds ranges from 0.025 to 0.04 K·m·s^{-1}. The increased CR winds destroy the SC and reduce the advection to about 0.015 K·m·s^{-1}. The advection effect is one of the main reasons for underestimation of the energy, resulting in a phase lag

between the vertical wind direction and the atmospheric scalar (Gao et al., 2017). Meanwhile, Figure 7 shows that the dispersive flux ranges from 0.01 to 0.025 K·m·s^{-1} under PR winds, and is reduced to near zero when CR winds are stronger than 2 m·s^{-1}, which is consistent with the results of Margairaz et al. (2020) that the dispersive heat flux becomes negligible at large wind speed where shear dominates the flow dynamics. On the contrary, SC decreases the turbulent energy flux as shown in Figure 7g–i.

The correlation between the SC and the dispersive and turbulent part of the energy fluxes demonstrates the impact of the ambient wind on the SEB. However, the CBL properties differ under various wind directions, which increases the difficulty of parameterizing this small-scale process at the coarse scale on the order of kilometres used in weather and climate models.
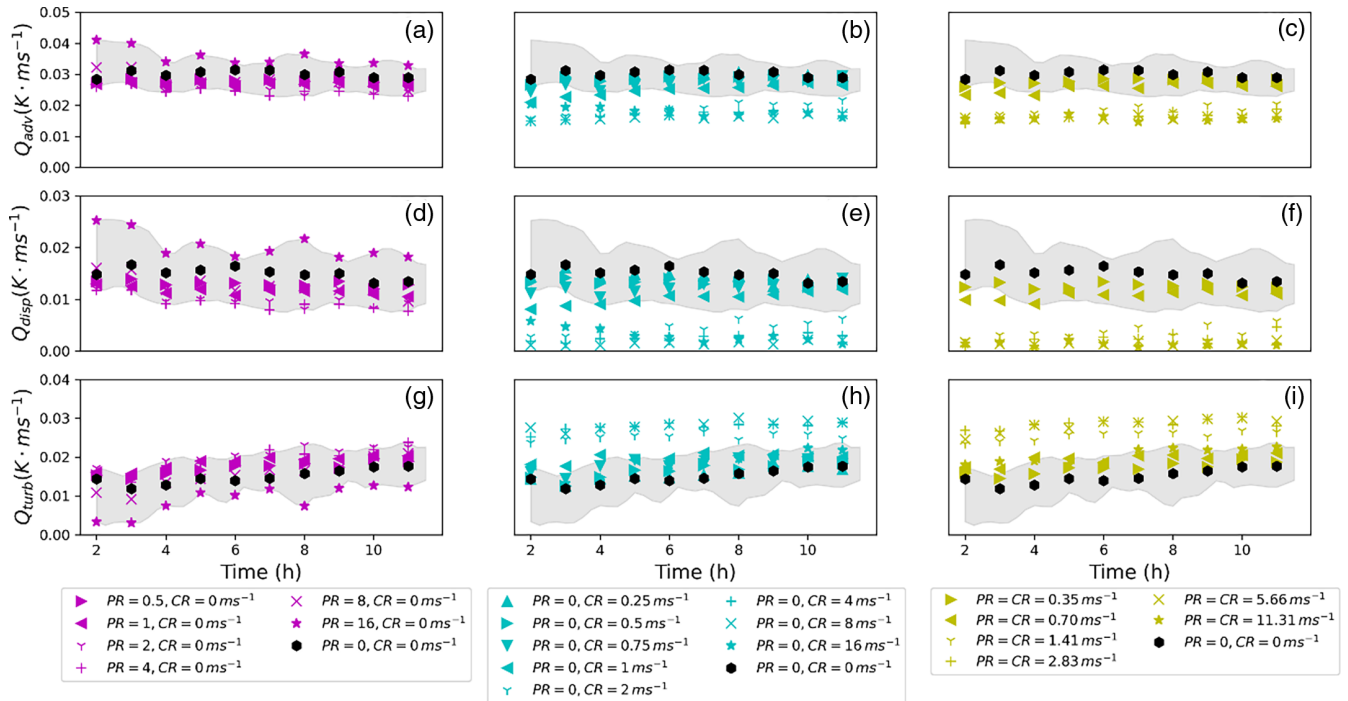
FIGURE 7 Domain-averaged temporal evolution of advection, dispersive and turbulent energy flux at the lowest atmosphere layer. Advection flux is in the top row, the grey shadow is the range for the simulation with only parallel-river (PR) wind. The middle and bottom rows are dispersive heat flux and resolved turbulent energy flux, respectively. The first column shows simulations under PR winds, the second column simulations under cross-river (CR) winds and the third column simulations under mixed winds [Colour figure can be viewed at wileyonlinelibrary.com]

3.3 | Vertical structure of the CBL

Studies have shown that surface heterogeneities influence the vertical profile of atmospheric states, which is more pronounced under a well-formed SC condition. (Hadfield *et al.*, 1992; Patton *et al.*, 2005; Huang and Margulis, 2009; Han *et al.*, 2019a). We decompose the wind into three parts based on Equation 7 to study the impact of ambient winds in conjunction with surface heterogeneity on the CBL.

Much of the early work uses either the root-mean-square (Bever and MacWilliams, 2016) or the variance of the mesoscale wind ($\sigma^2_{\text{w-phase}}$) (Han *et al.*, 2019b; Patton *et al.*, 2005) to determine the SC strength. We use the maximum value of the mesoscale vertical wind variance $Max\left(\sigma^2_{\text{w-phase}}\right)$ to represent the SC strength in the present work. In Figure 8, the ambient winds affect vertical and horizontal wind variance, while $Max\left(\sigma^2_{\text{w-phase}}\right)$ decreases from 0.58 to 0.25 m²s⁻² with increasing PR wind from 0 to 16 m·s⁻¹. On the other hand, $Max\left(\sigma^2_{\text{w-phase}}\right)$ decreases to near zero when CR wind is larger than 2 m·s⁻¹; this relates to the SC strength in Figures 3, 4, the larger the $Max\left(\sigma^2_{\text{w-phase}}\right)$, the stronger the SC. Ambient winds have a similar impact on the

mesoscale horizontal wind variance, which decreases the two peaks at the near-surface layer and the inversion layer at the top of the CBL. However, there is no obvious relationship between $\sigma^2_{\text{v-phase}}$ and SC strength. A typical peak value of $\sigma^2_{w'}$ usually appears at the height of Z/Z_i = 0.3 under free-cloud daytime conditions (Stull, 1988); in our simulations, the peak value of $\sigma^2_{w'}$ appears between Z/Z_i = 0.25 to 1.0 under different ambient winds.

The spatial mean potential temperature profile does not reflect the impact of the ambient wind, which is consistent with the findings by (Kim *et al.*, 2004). There are minor differences in the spatial pattern of potential temperature under different wind conditions (in supplementary material, Figure S4). The CR wind transports warm-dry air over the wet-cold region with strong blending effects compared to the simulation under the PR wind condition. With the increased wind speed, the potential temperature pattern transition from the cellular structure to the roll-like pattern (Poll *et al.*, 2017; Salesky *et al.*, 2017).

The mesoscale vertical wind variance profile describes the structure of the SC, which can be used as an indicator of the strength of the SC. It provides a potential quantitative perspective to study SC strength with scaling parameters in the next section.
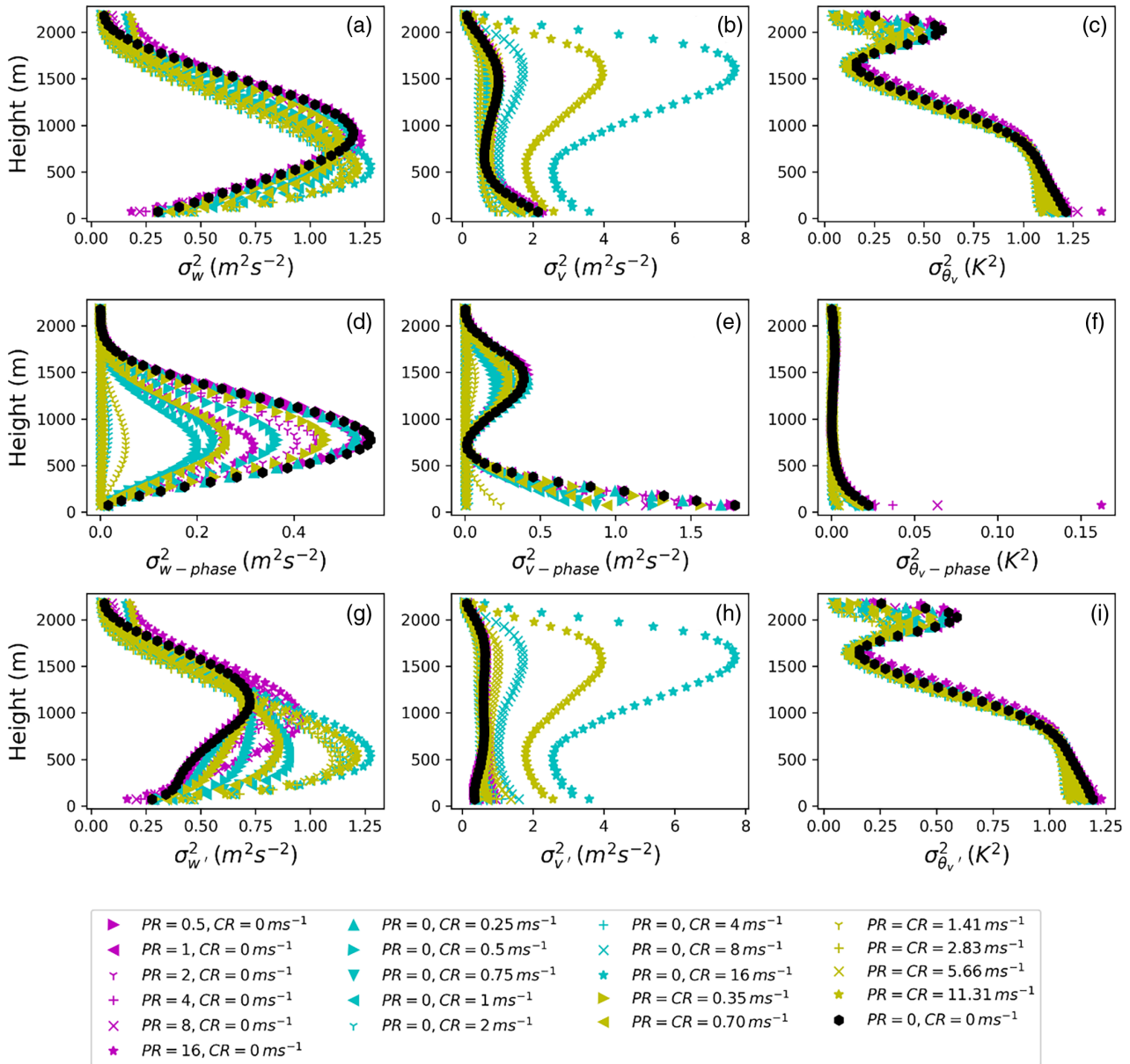
FIGURE 8 Vertical profile of variance over the period 1–12 h for vertical wind (first column), horizontal wind (second column), and virtual potential temperature (third column). The total variance (first row) is decomposed into mesoscale variance (second row) and turbulence variance (third row). The black symbol represents the reference simulation. CR, cross-river wind speed; PR, parallel-river wind speed [Colour figure can be viewed at wileyonlinelibrary.com]

3.4 | Similarity analysis

Since $Max\left(\sigma^2_{\text{w-phase}}\right)$ provides a measure of SC strength, this section examines the quantitative relationship between the normalized $Max\left(\sigma^2_{\text{w-phase}}\right)$, and the Bowen ratio, the stability parameter $(-Z_i/L)$, and the thermal heterogeneity parameter via dimensional analysis.

Figure 9a does not show a clear relationship between the domain-averaged Bowen ratio and the PR winds; any dependence comes from the CR winds only. The reference simulation has the largest $Max\left(\sigma^2_{\text{w-phase}}\right)/w^2_*$. When

CR $= 0$ m·s^{-1}, $Max\left(\sigma^2_{\text{w-phase}}\right)/w^2_*$ ranges between 0.20 and 0.51, and when CR $= 0.75$ m·s^{-1}, $Max\left(\sigma^2_{\text{w-phase}}\right)/w^2_*$ ranges between 0.15 and 0.21. In Figure 9b, it is evident that increasing CR wind decreases the domain-averaged Bowen ratio and $Max\left(\sigma^2_{\text{w-phase}}\right)/w^2_*$, accompanied by a positive correlation between the Bowen ratio and $Max\left(\sigma^2_{\text{w-phase}}\right)/w^2_*$.

Performing the same analyses of $Max\left(\sigma^2_{\text{w-phase}}\right)/w^2_*$ with $-Z_i/L$, the result shows that $-Z_i/L$ is dominated by the CR wind only. In Figure 9c, $-Z_i/L$ increases with the
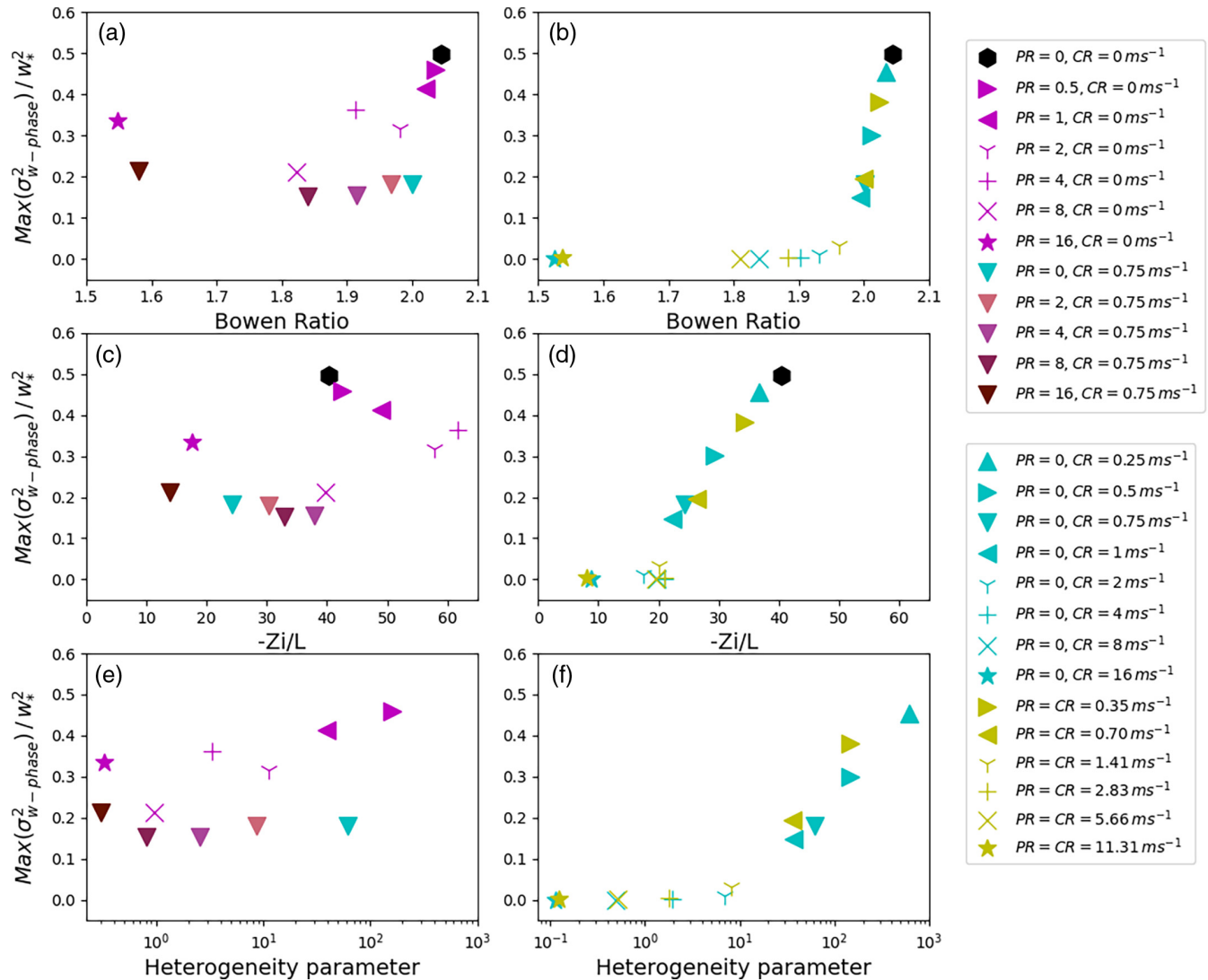
FIGURE 9 Relationship between the domain-averaged scaling parameter (Bowen ratio, $-Z_i/L$, heterogeneity parameter) and $Max\left(\sigma_{w\text{-phase}}^2\right)/w_*^2$ over the period of 1–12 h. [Left column: varying parallel-river (PR) wind and fixed cross-river (CR) wind (PR > 0, CR = 0, 0.75 m·s^{-1}); right column: varying CR wind (PR = 0, CR > 0 m·s^{-1}) and mixed wind (PR = CR > 0 m·s^{-1})]. The black symbol represents the reference simulation [Colour figure can be viewed at wileyonlinelibrary.com]

increase of PR wind and decreases when PR > 4 m·s^{-1}. This non-linear relationship applies to simulations with a fixed CR wind of 0.75 m·s^{-1}. Figure 9d shows a clear positive relationship between $-Z_i/L$ and $Max\left(\sigma_{w\text{-phase}}^2\right)/w_*^2$. The increasing CR wind decreases $-Z_i/L$, accompanied by the decrease of $Max\left(\sigma_{w\text{-phase}}^2\right)/w_*^2$.

Figure 9e, f show that the relationship between $Max\left(\sigma_{w\text{-phase}}^2\right)/w_*^2$ and the thermal heterogeneity parameter is consistent with the results obtained for the stability parameter and Bowen ratio. The relationship is weak under PR wind conditions but becomes strongly positive under CR wind conditions. Under CR wind conditions, the SC structure is destroyed when the heterogeneity

parameter is less than 7. The heterogeneity parameter threshold that distinguishes SC disappearance is related to the heterogeneity scale, but the positive correlation between the SC strength and the heterogeneity parameter remains clear.

Figure 9 suggests a threshold of CR = 2 m·s^{-1} for destroying the SC structure, where $Max\left(\sigma_{w\text{-phase}}^2\right)/w_*^2$ approaches zero. This result is close to that of Lee et al. (2019), who also identified a threshold value of 2 m·s^{-1} in their simulations, even though they used a different land surface heterogeneity pattern (i.e., checkerboard). The wind speed threshold seems smaller than the 5 m·s^{-1} from Avissar and Schmidt (1998) and 6 m·s^{-1} from Eder et al. (2015). The wind values could be affected

by the surface heat flux amplitude, which is 0.2 K·m·s⁻¹ in Avissar and Schmidt (1998), and 0.24 K·m·s⁻¹ in Eder *et al.* (2015). The amplitude in our reference simulation is 0.14 K·m·s⁻¹, which is closer to the 0.10 K·m·s⁻¹ (approx. 126 W·m⁻²) in the study of Lee *et al.* (2019). On the other hand, the land surface heterogeneity scale also affects the SC strength. The magnitude of the wind speed threshold varies with the different model settings.

A scaling parameter approach has been applied to close the SEB gap, considering only atmospheric stability and thermal heterogeneity parameters (De Roo *et al.*, 2018; Wanner *et al.*, 2021). Semi-empirical models derived from LES results with the checkerboard heterogeneity in their study have been tested on measurements and significantly improved the SEB gap, even though no wind direction is considered (Mauder *et al.*, 2021). The relationship in Figure 9 shows the importance of the relative orientation between the heterogeneous surface and the wind direction for SC formation, highlighting the difficulty of incorporating wind direction into the parameterization. Nevertheless, the proposed similarity analysis and scaling method provide a new quantitative perspective to study the effect of ambient wind on SC under heterologous soil moisture conditions.

4 | SUMMARY AND CONCLUSION

In this study, we investigate the impact of ambient wind on CBL by performing various large-eddy simulations with coupled ICON-LEM and TERRA-ML. All simulations utilize the same idealized atmospheric condition except for the different ambient wind speeds and wind directions over a flat river corridor mimicked by a heterogeneous soil moisture distribution.

The SC structure is well organized under the reference simulation and remains under strong PR wind but is destroyed when the CR wind is larger than 2 m·s⁻¹. Ambient wind and soil moisture dominate the surface energy distribution independent of wind direction, while in the atmospheric surface layer SC decreases the turbulent energy flux and increases the advection and dispersive heat flux, indicating the importance of SC on the SEB.

The vertical profile of wind variance measures SC, and we use the maximum value of mesoscale vertical wind variance as a quantitative indicator of SC strength. Based on the dimensional analysis, the normalized $Max\left(\sigma^2_{\text{w-phase}}\right)$ has a positive relationship with the Bowen ratio, stability parameter ($-Z_i/L$), and thermal heterogeneity parameter. The relationship between the normalized phase wind and the scaling parameters shows the

importance of the relative orientation between the heterogeneous surface and the wind direction for SC formation. The clear relationship of SC strength with scaling parameters provides a new quantitative perspective on studying the effect of ambient winds on SC, which should be further explored in the future by measurements.

With this work, we comprehensively studied the influence of ambient wind on CBL development, especially on the formation of SC and its impact on the essential bulk statistics. The non-linear impact of the ambient wind suggests that it is still a significant challenge to parameterize SC in coarse-scale numerical weather prediction and climate models, which remains the subject of ongoing and future research.

ORCID
Lijie Zhang https://orcid.org/0000-0002-8214-2488
Stefan Poll https://orcid.org/0000-0003-2527-0747
Stefan Kollet https://orcid.org/0000-0003-0095-1554

REFERENCES

Avissar, R. and Schmidt, T. (1998) An evaluation of the scale at which ground-surface heat flux patchiness affects the convective boundary layer using large-Eddy simulations. *Journal of the Atmospheric Sciences*, 55, 2666–2689. https://doi.org/10.1175/1520-0469(1998)055<2666:AEOTSA>2.0.CO;2

Behrendt A, Wulfmeyer V, Turner DD, LAFE Team (2018) Initial results of the Land-Atmosphere Feedback Experiment (LAFE). 20th EGU General Assembly, EGU2018, Proceedings from the conference held 4-13 April, 2018 in Vienna, Austra, p 12542.

Bever, A.J. and MacWilliams, M.L. (2016) Factors influencing the calculation of periodic secondary circulation in a tidal river: numerical modelling of the lower Sacramento River, USA. *Hydrological Processes*, 30, 995–1016. https://doi.org/10.1002/hyp.10690

Beyrich, F. and Mengelkamp, H.-T. (2006) Evaporation over a heterogeneous land surface: EVA_GRIPS and the LITFASS-2003 experiment—an overview. *Boundary-Layer Meteorology*, 121, 5–32. https://doi.org/10.1007/s10546-006-9079-z

Butterworth, B.J., Desai, A.R., Metzger, S., et al. (2021) Connecting land–atmosphere interactions to surface heterogeneity in CHEESEHEAD19. *Bulletin of the American Meteorological Society*, 102, E421–E445. https://doi.org/10.1175/BAMS-D-19-0346.1

Cioni, G. and Hohenegger, C. (2017) Effect of soil moisture on diurnal convection and precipitation in large-Eddy simulations. *Journal of Hydrometeorology*, 18, 1885–1903. https://doi.org/10.1175/JHM-D-16-0241.1

Davin, E.L., Stöckli, R., Jaeger, E.B., Levis, S. and Seneviratne, S.I. (2011) COSMO-CLM2: a new version of the COSMO-CLM model coupled to the community land model. *Climate Dynamics*, 37, 1889–1907. https://doi.org/10.1007/s00382-011-1019-z

Deardorff, J.W. (1970). Convective Velocity and Temperature Scales for the Unstable Planetary Boundary Layer and for Rayleigh Convection. *Journal of the Atmospheric Sciences*, 27(8), 1211–1213. https://doi.org/10.1175/1520-0469(1970)027<1211:CVATSF>2.0.CO;2

De Roo, F., Zhang, S., Huq, S. and Mauder, M. (2018) A semi-empirical model of the energy balance closure in the surface layer. *PLoS One*, 13, 1–23. https://doi.org/10.1371/journal.pone.0209022

Dickinson, R.E. (1984) Modeling evapotranspiration for three-dimensional global climate models. In: *Climate Processes and Climate Sensitivity*. Washington, D. C: American Geophysical Union, pp. 58–72. https://doi.org/10.1029/GM029p0058

Ding, M. and Tong, C. (2021) Multi-point Monin–Obukhov similarity of turbulence Cospectra in the convective atmospheric boundary layer. *Boundary-Layer Meteorology*, 178, 185–199. https://doi.org/10.1007/s10546-020-00571-4

Dipankar, A., Stevens, B., Heinze, R., Moseley, C., Zängl, G., Giorgetta, M. and Brdar, S. (2015) Large eddy simulation using the general circulation model ICON. *Journal of Advances in Modeling Earth Systems*, 6, 963–986. https://doi.org/10.1002/2015MS000431

Dupont, S. and Patton, E.G. (2012) Momentum and scalar transport within a vegetation canopy following atmospheric stability and seasonal canopy changes: the CHATS experiment. *Atmospheric Chemistry and Physics*, 12, 5913–5935. https://doi.org/10.5194/acp-12-5913-2012

Eder, F., De Roo, F., Rotenberg, E., et al. (2015) Secondary circulations at a solitary forest surrounded by semi-arid shrubland and their impact on eddy-covariance measurements. *Agricultural and Forest Meteorology*, 211–212, 115–127. https://doi.org/10.1016/j.agrformet.2015.06.001

Foken, T. (2006) 50 years of the Monin–Obukhov similarity theory. *Boundary-Layer Meteorology*, 119, 431–447. https://doi.org/10.1007/s10546-006-9048-6

Foken, T., Mauder, M., Liebethal, C., Wimmer, F., Beyrich, F., Leps, J.P., Raasch, S., DeBruin, H.A.R., Meijninger, W.M.L. and Bange, J. (2010) Energy balance closure for the LITFASS-2003 experiment. *Theoretical and Applied Climatology*, 101, 149–160. https://doi.org/10.1007/s00704-009-0216-8

Fortuniak, K., Pawlak, W. and Siedlecki, M. (2013) Integral turbulence statistics over a central European city Centre. *Boundary-Layer Meteorology*, 146, 257–276. https://doi.org/10.1007/s10546-012-9762-1

Franssen, H.J.H., Stöckli, R., Lehner, I., Rotenberg, E. and Seneviratne, S.I. (2010) Energy balance closure of eddy-covariance data: a multisite analysis for European FLUXNET stations. *Agricultural and Forest Meteorology*, 150, 1553–1567. https://doi.org/10.1016/j.agrformet.2010.08.005

Gao, Z., Liu, H., Katul, G.G. and Foken, T. (2017) Non-closure of the surface energy balance explained by phase difference between vertical velocity and scalars of large atmospheric eddies. *Environmental Research Letters*, 12(3), 034025. https://doi.org/10.1088/1748-9326/aa625b.

Grasselt, R., Schüttemeyer, D., Warrach-Sagi, K., Ament, F. and Simmer, C. (2008) Validation of TERRA-ML with discharge measurements. *Meteorologische Zeitschrift*, 17, 763–773. https://doi.org/10.1127/0941-2948/2008/0334

Hadfield, M.G., Cotton, W.R. and Pielke, R.A. (1992) Large-eddy simulations of thermally forced circulations in the convective boundary layer. Part II: the effect of changes in wavelength and wind speed. *Boundary-Layer Meteorology*, 58, 307–327. https://doi.org/10.1007/BF00120235

Han, C., Brdar, S. and Kollet, S. (2019a) Response of convective boundary layer and shallow cumulus to soil moisture heterogeneity: a large-eddy simulation study. *Journal of Advances in Modeling Earth Systems*, 11, 4305–4322. https://doi.org/10.1029/2019MS001772

Han, C., Brdar, S., Raasch, S. and Kollet, S. (2019b) Large-eddy simulation of catchment-scale circulation. *Quarterly Journal of the Royal Meteorological Society*, 145, 1218–1233. https://doi.org/10.1002/qj.3491

Hatlee, S.C. and Wyngaard, J.C. (2007) Improved subfilter-scale models from the HATS field data. *Journal of the Atmospheric Sciences*, 64, 1694–1705. https://doi.org/10.1175/JAS3909.1

Heinze, R., Dipankar, A., Henken, C.C., Moseley, C., Sourdeval, O., Trömel, S., Xie, X., Adamidis, P., Ament, F., Baars, H., Barthlott, C., Behrendt, A., Blahak, U., Bley, S., Brdar, S., Brueck, M., Crewell, S., Deneke, H., di Girolamo, P., Evaristo, R., Fischer, J., Frank, C., Friederichs, P., Göcke, T., Gorges, K., Hande, L., Hanke, M., Hansen, A., Hege, H.C., Hoose, C., Jahns, T., Kalthoff, N., Klocke, D., Kneifel, S., Knippertz, P., Kuhn, A., van Laar, T., Macke, A., Maurer, V., Mayer, B., Meyer, C.I., Muppa, S.K., Neggers, R.A.J., Orlandi, E., Pantillon, F., Pospichal, B., Röber, N., Scheck, L., Seifert, A., Seifert, P., Senf, F., Siligam, P., Simmer, C., Steinke, S., Stevens, B., Wapler, K., Weniger, M., Wulfmeyer,

V., Zängl, G., Zhang, D. and Quaas, J. (2017) Large-eddy simulations over Germany using ICON: a comprehensive evaluation. *Quarterly Journal of the Royal Meteorological Society*, 143, 69–100. https://doi.org/10.1002/qj.2947

Holtslag, A.A.M. and Nieuwstadt, F.T.M. (1986) Scaling the atmospheric boundary layer. *Boundary-Layer Meteorology*, 36, 201–209. https://doi.org/10.1007/BF00117468

Huang, H.Y. and Margulis, S.A. (2009) On the impact of surface heterogeneity on a realistic convective boundary layer. *Water Resources Research*, 45, 1–16. https://doi.org/10.1029/2008WR007175

Kanda, M., Inagaki, A., Letzel, M.O., Raasch, S. and Watanabe, T. (2004) LES study of the energy imbalance problem with Eddy covariance fluxes. *Boundary-Layer Meteorology*, 110, 381–404. https://doi.org/10.1023/B:BOUN.0000007225.45548.7a

Kang, S.-L. (2009) Temporal oscillations in the convective boundary layer forced by mesoscale surface heat-flux variations. *Boundary-Layer Meteorology*, 132, 59–81. https://doi.org/10.1007/s10546-009-9391-5

Kang, S.-L. and Bryan, G.H. (2011) A large-Eddy simulation study of moist convection initiation over heterogeneous surface fluxes. *Monthly Weather Review*, 139, 2901–2917. https://doi.org/10.1175/MWR-D-10-05037.1

Kang, S.-L., Davis, K.J. and LeMone, M. (2007) Observations of the ABL structures over a heterogeneous land surface during IHOP_2002. *Journal of Hydrometeorology*, 8, 221–244. https://doi.org/10.1175/JHM567.1

Kang, S.-L. and Lenschow, D.H. (2014) Temporal evolution of low-level winds induced by two-dimensional mesoscale surface heat-flux heterogeneity. *Boundary-Layer Meteorology*, 151, 501–529. https://doi.org/10.1007/s10546-014-9912-8

Kim, H.-J., Noh, Y. and Raasch, S. (2004) Interaction between wind and temperature fields in the planetary boundary layer for a spatially heterogeneous surface heat flux. *Boundary-Layer Meteorology*, 111, 225–246. https://doi.org/10.1023/B:BOUN.0000016471.75325.75

Lee, J.M., Zhang, Y. and Klein, S.A. (2019) The effect of land surface heterogeneity and background wind on shallow cumulus clouds and the transition to deeper convection. *Journal of the Atmospheric Sciences*, 76, 401–419. https://doi.org/10.1175/JAS-D-18-0196.1

Letzel, M.O. and Raasch, S. (2003) Large Eddy simulation of thermally induced oscillations in the convective boundary layer. *Journal of the Atmospheric Sciences*, 60, 2328–2341. https://doi.org/10.1175/1520-0469(2003)060<2328:LESOTI>2.0.CO;2

Lilly, D.K. (1962) On the numerical simulation of buoyant convection. *Tellus*, 14, 148–172. https://doi.org/10.1111/j.2153-3490.1962.tb00128.x

Macke, A., Seifert, P., Baars, H., Barthlott, C., Beekmans, C., Behrendt, A., Bohn, B., Brueck, M., Bühl, J., Crewell, S., Damian, T., Deneke, H., Düsing, S., Foth, A., di Girolamo, P., Hammann, E., Heinze, R., Hirsikko, A., Kalisch, J., Kalthoff, N., Kinne, S., Kohler, M., Löhnert, U., Madhavan, B.L., Maurer, V., Muppa, S.K., Schween, J., Serikov, I., Siebert, H., Simmer, C., Späth, F., Steinke, S., Träumner, K., Trömel, S., Wehner, B., Wieser, A., Wulfmeyer, V. and Xie, X. (2017) The HD(CP)² observational prototype experiment (HOPE)–an overview. *Atmospheric Chemistry and Physics*, 17, 4887–4914. https://doi.org/10.5194/acp-17-4887-2017

Margairaz, F., Pardyjak, E.R. and Calaf, M. (2020) Surface thermal heterogeneities and the atmospheric boundary layer: the thermal heterogeneity parameter. *Boundary-Layer Meteorology*, 177, 49–68. https://doi.org/10.1007/s10546-020-00544-7

Mauder, M., Foken, T. and Cuxart, J. (2020) Surface-energy-balance closure over land: a review. *Boundary-Layer Meteorology*, 177, 395–426. https://doi.org/10.1007/s10546-020-00529-6

Mauder, M., Ibrom, A., Wanner, L., de Roo, F., Brugger, P., Kiese, R. and Pilegaard, K. (2021) Options to correct local turbulent flux measurements for large-scale fluxes using an approach based on large-eddy simulation. *Atmospheric Measurement Techniques*, 14, 7835–7850. https://doi.org/10.5194/amt-14-7835-2021

Morrison, T., Pardyjak, E.R., Mauder, M. and Calaf, M. (2022) The heat-flux imbalance: the role of advection and dispersive fluxes on heat transport over thermally heterogeneous terrain. *Boundary-Layer Meteorology*, 183, 227–247. https://doi.org/10.1007/s10546-021-00687-1

Oncley, S.P., Foken, T., Vogt, R., Kohsiek, W., DeBruin, H.A.R., Bernhofer, C., Christen, A., Gorsel, E., Grantz, D., Feigenwinter, C., Lehner, I., Liebethal, C., Liu, H., Mauder, M., Pitacco, A., Ribeiro, L. and Weidinger, T. (2007) The energy balance experiment EBEX-2000. Part I: overview and energy balance. *Boundary-Layer Meteorology*, 123, 1–28. https://doi.org/10.1007/s10546-007-9161-1

Patton, E.G., Sullivan, P.P. and Moeng, C.-H. (2005) The influence of idealized heterogeneity on wet and dry planetary boundary layers coupled to the land surface. *Journal of the Atmospheric Sciences*, 62, 2078–2097. https://doi.org/10.1175/JAS3465.1

Pielke, R.A., Sr. (2001) Influence of the spatial distribution of vegetation and soils on the prediction of cumulus convective rainfall. *Reviews of Geophysics*, 39, 151–177. https://doi.org/10.1029/1999RG000072

Poll, S., Shrestha, P. and Simmer, C. (2017) Modelling convectively induced secondary circulations in the terra incognita with TerrSysMP. *Quarterly Journal of the Royal Meteorological Society*, 143, 2352–2361. https://doi.org/10.1002/qj.3088

Poll, S., Shrestha, P. and Simmer, C. (2022) Grid resolution dependency of land surface heterogeneity effects on boundary-layer structure. *Quarterly Journal of the Royal Meteorological Society*, 148, 141–158. https://doi.org/10.1002/qj.4196

Prabha, T.V., Karipot, A. and Binford, M.W. (2007) Characteristics of secondary circulations over an inhomogeneous surface simulated with large-eddy simulation. *Boundary-Layer Meteorology*, 123, 239–261. https://doi.org/10.1007/s10546-006-9137-6

Raasch, S. and Harbusch, G. (2001) An analysis of secondary circulations and their effects caused by small-scale surface inhomogeneities using large-Eddy simulation. *Boundary-Layer Meteorology*, 101, 31–59. https://doi.org/10.1023/A:1019297504109

Rihani, J.F., Chow, F.K. and Maxwell, R. (2015) Isolating effects of terrain and soil moisture heterogeneity on the atmospheric boundary layer: Idealized simulations to diagnose land-atmosphere feedbacks. *Journal of Advances in Modeling Earth Systems.*, 7, 915–937. https://doi.org/10.1002/2014MS000371

Salesky, S.T., Chamecki, M. and Bou-Zeid, E. (2017) On the nature of the transition between roll and cellular organization in the convective boundary layer. *Boundary-Layer Meteorology*, 163, 41–68. https://doi.org/10.1007/s10546-016-0220-3

Schrodin, R. and Heise, E. (2001) *The Multi-Layer Version of the DWD Soil Model TERRA-LM*. DWD, Offenbach, Germany. https://doi.org/10.5676/DWD_pub/nwv/cosmo-tr_2

Schulz, J.-P., Dümenil, L., Polcher, J., Schlosser, C.A. and Xue, Y. (1998) Land surface energy and moisture fluxes: comparing three models. *Journal of Applied Meteorology and Climatology*, 37, 288–307. https://doi.org/10.1175/1520-0450(1998)037<0288:LSEAMF>2.0.CO;2

Schulz, J.-P. and Vogel, G. (2020) Improving the processes in the land surface scheme TERRA: bare soil evaporation and skin temperature. *Atmosphere*, 11, 513. https://doi.org/10.3390/atmos11050513

Schumann, U. (1991) A simple model of the convective boundary layer over wavy terrain with variable heat flux. *Beitraege zur Physik der Atmosphaere*, 64, 169–184. https://elib.dlr.de/31606/

Sedlar, J., Riihimaki, L.D., Turner, D.D., Duncan, J., Adler, B., Bianco, L., Lantz, K., Wilczak, J., Hall, E., Herrera, C. and Hodges, G.B. (2022) Investigating the impacts of daytime boundary layer clouds on surface energy fluxes and boundary layer structure during CHEESEHEAD19. *Journal of Geophysical Research, D: Atmospheres*, 127, 1–24. https://doi.org/10.1029/2021JD036060

Shen, L., Sun, J., Yuan, R. and Liu, P. (2016) Characteristics of secondary circulations in the convective boundary layer over two-dimensional heterogeneous surfaces. *Journal of Meteorological Research*, 30, 944–960. https://doi.org/10.1007/s13351-016-6016-z

Stamnas, E., Lammert, A., Winkelmann, V. and Lang, U. (2016) The HD(CP)2 data archive for atmospheric measurement data. *ISPRS International Journal of Geo-Information*, 5, 124. https://doi.org/10.3390/ijgi5070124

Stoll, R., Gibbs, J.A., Salesky, S.T., Anderson, W. and Calaf, M. (2020) Large-Eddy simulation of the atmospheric boundary layer. *Boundary-Layer Meteorology*, 177, 541–581. https://doi.org/10.1007/s10546-020-00556-3

Stull, R.B. (1988) *An Introduction to Boundary Layer Meteorology*. Dordrecht: Springer. https://doi.org/10.1007/978-94-009-3027-8

van Heerwaarden, C.C. and de Arellano, J.V.G. (2008) Relative humidity as an indicator for cloud formation over heterogeneous land surfaces. *Journal of the Atmospheric Sciences*, 65, 3263–3277. https://doi.org/10.1175/2008JAS2591.1

Wan, H., Giorgetta, M.A., Zängl, G., Restelli, M., Majewski, D., Bonaventura, L., Fröhlich, K., Reinert, D., Rípodas, P., Kornblueh, L. and Förstner, J. (2013) The ICON-1.2 hydrostatic atmospheric dynamical core on triangular grids – part 1: formulation and performance of the baseline version. *Geoscientific Model Development*, 6, 735–763. https://doi.org/10.5194/gmd-6-735-2013

Wanner L, Calaf M, Mauder M (2021) Incorporating the effect of heterogeneous surface heating into a semi-empirical model of the surface energy balance closure. *PLOS ONE*, 17(6): e0268097–21. https://doi.org/10.1371/journal.pone.0268097

Wanner, L., De Roo, F., Sühring, M. and Mauder, M. (2022) How does the choice of the lower boundary conditions in large-Eddy simulations affect the development of dispersive fluxes near the surface? *Boundary-Layer Meteorology*, 182, 1–27. https://doi.org/10.1007/s10546-021-00649-7

Weber, R.O. (1999) Remarks on the definition and estimation of friction velocity. *Boundary-Layer Meteorology*, 93, 197–209. https://doi.org/10.1023/A:1002043826623

Weckwerth, T.M., Parsons, D.B., Koch, S.E., Moore, J.A., LeMone, M.A., Demoz, B.B., Flamant, C., Geerts, B., Wang, J. and Feltz, W.F. (2004) An overview of the international H2O project (IHOP_2002) and some preliminary highlights. *Bulletin of the American Meteorological Society*, 85, 253–278. https://doi.org/10.1175/BAMS-85-2-253

Zängl, G., Reinert, D., Rípodas, P. and Baldauf, M. (2015) The ICON (ICOsahedral non-hydrostatic) modelling framework of DWD and MPI-M: description of the non-hydrostatic dynamical core. *Quarterly Journal of the Royal Meteorological Society*, 141, 563–579. https://doi.org/10.1002/qj.2378

SUPPORTING INFORMATION

Additional supporting information can be found online in the Supporting Information section at the end of this article.